

Fermi arcs, pseudogap and collective excitations in doped Sr_2IrO_4 : A generalized fluctuation exchange study

Hu Wang, Shun-Li Yu, and Jian-Xin Li

*National Laboratory of Solid State Microstructures and Department of Physics, Nanjing University, Nanjing 210093, China
Collaborative Innovation Center of Advanced Microstructures, Nanjing University, Nanjing, China*

(Dated: April 20, 2015)

Motivated by recent experimental measurements, we study the quasiparticle spectra and the collective excitations in doped Sr_2IrO_4 , in which the interesting interplay between the electronic correlations and strong spin-orbital coupling (SOC) exists. To include the SOC, we use the Hugenholtz diagrams to extend the fluctuation exchange (FLEX) approach to the case where the $\text{SU}(2)$ symmetry can be broken. By using this generalized FLEX method, we find a weak pseudogap behavior near $(\pi, 0)$ in the slightly electron-doped system, with the corresponding Fermi arc formed by the partial destruction of Fermi surface. Similar features also appear in the hole-doped system, however, the position of the Fermi arc is rotated 45° with respect to the former. These results are consistent with the recent angle-resolved photoemission spectra in Sr_2IrO_4 . We elaborate that these anomalous phenomena are caused by the scatterings of quasiparticles off the isospin fluctuation derived from the effective $J_{\text{eff}} = 1/2$ doublet.

PACS numbers: 71.27.+a, 71.70.Ej, 71.10.-w, 71.18.+y

I. INTRODUCTION

Recently, the $5d$ transition-metal iridium oxides have attracted significant attention, because they exhibit a number of exotic phenomena induced by the spin-orbital coupling (SOC) and the correlation effects of electrons^{1,2}. Of these iridates, Sr_2IrO_4 of particular interest for it shares many analogies with the parent compound La_2CuO_4 of high- T_c cuprate superconductors, such as the same layered perovskite crystal structure³, the same antiferromagnetic (AFM) insulating ground state⁴, the similar magnetic excitation spectrum⁵ and electronic structure⁶. It has also been proposed theoretically to realize the unconventional superconductivity via doping⁷.

In particular, the recent angle-resolved-photoemission-spectroscopy (ARPES) measurements on the slightly electron-doped Sr_2IrO_4 show a temperature-dependent pseudogap phenomenon⁸. The intensity of the spectra is much suppressed in an extended region near $(0, \pi)$, resulting in the Fermi arc which resembles the case in the hole-doped cuprates⁹. For the slightly hole-doped Sr_2IrO_4 , another ARPES experiment also exhibits the trait of pseudogap¹⁰, but with the suppression of spectral near the $(\pi/2, \pi/2)$ point. As the pseudogap puzzle is the longstanding unsolved problem in cuprate superconductors, studying the origin of the Fermi arcs and pseudogaps in doped Sr_2IrO_4 is not only important for this material itself, but might also help to investigate the similar phenomena in high- T_c cuprates and/or other materials.

Sr_2IrO_4 shows a multi-orbital electronic structure where the t_{2g} and e_g orbitals are separated by large crystal field. The five electrons (one hole) reside in the lower t_{2g} manifold of xy, xz, yz orbitals. In spite of the large band width and small Coulomb interactions, Sr_2IrO_4 is an antiferromagnetic insulator^{3,4}. It has been proposed that the SOC breaks this sixfold degenerate manifold

into completely filled $J_{\text{eff}} = 3/2$ bands and a half-filled $J_{\text{eff}} = 1/2$ band (Kramers doublet) which is further split by the relatively small Coulomb interactions. Thus, it can be simplified to an effective one-band half-filled system, which hosts an isospin $J_{\text{eff}} = 1/2$ spin-orbital Mott insulating ground state^{11,12}. However, the validity of this isospin $J_{\text{eff}} = 1/2$ Mott picture including its robustness to dopings still remains an open question^{13–16}.

Motivated by these experimental and theoretical progress, we carry out a theoretical study of the collective excitations and quasiparticle spectra in the doped Sr_2IrO_4 , based on the three-orbital Hubbard model with the inclusion of the SOC.

The multi-orbital structure together with the SOC confines the exact diagonalization and quantum Monte Carlo (QMC) methods to very small systems. In view of this, the fluctuation-exchange (FLEX) approximation is a good alternative^{17–19}. The FLEX method has advantages to handle various collective fluctuations, and the calculation results agree well with the QMC simulations for the Hubbard model with the moderate on-site interaction U ^{17,18}. Up to now, the FLEX approach has been extensively applied to the high- T_c cuprates²⁰, the iron-based superconductors²¹, and other correlated electron systems^{22,23}. However, the previous FLEX calculations are restricted to the case with the spin rotational invariance. In order to include the SOC, we will use the technique of Hugenholtz diagrams to extend the FLEX approach to more general cases, where the $\text{SU}(2)$ symmetry can be broken.

Based on this method, we find that the spectral function of quasiparticles is much suppressed at parts of momenta in the lightly doped region, suggesting the emergence of the pseudogap. Explicitly, the suppression occurs near $(0, \pi)$ point for slightly electron doping and thus leads to the Fermi arc near $(\pi/2, \pi/2)$, while their positions are reversed in the hole-doped side. These results

are consistent with the recent ARPES observations^{8,10}. We elaborate that the Fermi arcs and pseudogaps are mainly caused by the isospin fluctuation with momentum (π, π) , which overwhelms both the spin and orbital fluctuations. We have also studied the evolution of various collective fluctuations with doping and find that the isospin fluctuation dominates in the region from 30% hole-doping to 50% electron-doping. These results suggest that the scenario of $J_{\text{eff}} = 1/2$ spin-orbital Mott insulator is applicable to the parent and the extensively doped compounds of Sr_2IrO_4 .

II. MODEL AND METHOD

A. Three orbital Hubbard model

We begin with the t_{2g} three-orbital Hubbard model on the square lattice²⁴: $H = H_{\text{kin}} + H_{\text{SOC}} + H_I$. The kinetic and SOC Hamiltonians read

$$\begin{aligned} H_{\text{kin}} &= \sum_{\mathbf{k}m\alpha} \epsilon_m(\mathbf{k}) d_{\mathbf{k}m\alpha}^\dagger d_{\mathbf{k}m\alpha}, \\ H_{\text{SOC}} &= \sum_{\mathbf{k}mn\alpha\beta} \frac{\xi_{\text{SOC}}}{2} \mathbf{L}_{mn} \cdot \boldsymbol{\sigma}_{\alpha\beta} d_{\mathbf{k}m\alpha}^\dagger d_{\mathbf{k}n\beta}, \end{aligned} \quad (1)$$

where $d_{\mathbf{k}m\alpha}^\dagger$ ($d_{\mathbf{k}m\alpha}$) creates (annihilates) a m -orbital electron with spin α and momentum \mathbf{k} . ξ_{SOC} denotes the magnitude of SOC, and \mathbf{L} and $\boldsymbol{\sigma}$ are the orbital angular momentum operator and Pauli matrix. Explicitly, the nonzero elements of $\mathbf{L} = (L^x, L^y, L^z)$ for $yz(1)$, $zx(2)$, and $xy(3)$ orbitals are $L_{23}^x = -L_{32}^x = L_{31}^y = -L_{13}^y = L_{12}^z = -L_{21}^z = i$. The single-particle dispersions are given by $\epsilon_1(\mathbf{k}) = -2t_5 \cos k_x - 2t_4 \cos k_y$, $\epsilon_2(\mathbf{k}) = -2t_4 \cos k_x - 2t_5 \cos k_y$, and $\epsilon_3(\mathbf{k}) = -2t_1(\cos k_x + \cos k_y) - 4t_2 \cos k_x \cos k_y - 2t_3(\cos 2k_x + \cos 2k_y) + \mu_3$, with parameters $(t_2, t_3, t_4, t_5, \mu_3) = (0.5, 0.25, 1.03, 0.17, -1.0)t_1$ ²⁴. Hereafter, we set $\xi_{\text{SOC}} = 1.03 t_1$ without annotation, and $t_1 = 1$ as the energy unit. The interaction part on the l -site is given by

$$\begin{aligned} H_I(l) &= \frac{1}{2} \sum_{ijmn} \sum_{\alpha\beta\mu\nu} \delta_{\alpha\nu} \delta_{\beta\mu} \{ U \delta_{i=j=m=n} (1 - \delta_{\alpha\beta}) \\ &\quad + U' \delta_{in} \delta_{jm} (1 - \delta_{ij}) + J \delta_{im} \delta_{jn} (1 - \delta_{ij}) \\ &\quad + J' \delta_{ij} \delta_{mn} (1 - \delta_{im}) (1 - \delta_{\alpha\beta}) \} d_{li\alpha}^\dagger d_{lj\beta}^\dagger d_{lm\mu} d_{ln\nu}, \end{aligned} \quad (2)$$

where U (U') is the intra-orbital (inter-orbital) Coulomb interaction, J the Hund's coupling and J' the inter-orbital pair hopping. As usual, we set $J' = J$ and use the relation $U = U' + 2J$. Note that we have fabricated H_I to be a compact form to conveniently construct the Hugenholtz vertices.

B. Generalized FLEX method

In this section, we give a thorough introduction of the generalized FLEX method, which can naturally include the SOC term. The FLEX approach originates from the conserving approximation theory proposed by Baym and Kadanoff²⁵. In this formalism, the closed-linked Φ diagrams (also known as Luttinger-Ward functional²⁶) yield the self-energy and the irreducible interaction vertices in a thermodynamic self-consistent manner, in which the conservation laws on the particle number, momentum, angular momentum and energy are respected. The FLEX method pioneered by Bickers and Scalapino¹⁷ is the simplest application of the Baym-Kadanoff formalism beyond the Hartree-Fock level, and has been widely applied to the single- and multi-orbital Hubbard models¹⁹, in which the spin rotational invariance is respected. When the SU(2) spin symmetry is conserved, the scattering processes explicitly include the equal-spin particle-particle (PP), opposite-spin PP, equal-spin particle-hole (PH), and opposite-spin PH channels (see Ref.¹⁷). If the SU(2) symmetry is broken, however, one must consider the PP and PH fluctuations in a comprehensive manner for there are mixtures of equal-spin and opposite-spin scatterings.

We employ the Hugenholtz diagrams²⁷ to extend this method to the SU(2) broken cases. Considering the on-site two-body potential

$$\frac{1}{2} \sum_{ijmn} \langle ij|V|mn \rangle c_i^\dagger c_j^\dagger c_n c_m, \quad (3)$$

where the index i denote both the spin and orbital degrees of freedom. The Hugenholtz bare vertices for the PP and PH channels are defined as

$$\begin{aligned} \Gamma_{ij,mn}^p &\equiv \langle ij|V|mn \rangle - \langle ij|V|nm \rangle, \\ \Gamma_{ij,mn}^h &\equiv \Gamma_{in,jm}^p, \end{aligned} \quad (4)$$

and they are diagrammatically shown in Fig. 1 (a) and (b). The Hartree-Fock (HF) and the second order Φ diagrams can be drawn easily by the bare vertices [Fig. 1 (c) and (d)]. Connecting the bare PP or PH vertices in the random-phase-approximation (RPA) series by the Green's function \hat{G} , we get the main body of FLEX Φ diagrams, which is shown in Fig. 1 (e) and (f).

For the m -orbital system without SU(2) symmetry, the Green's function and the self-energy can be expressed as $2m \times 2m$ matrices, satisfying the Dyson equation,

$$\hat{G}(\mathbf{k}, i\mathbf{k}_n) = [i\mathbf{k}_n \hat{1} - \hat{h}(\mathbf{k}) - \hat{\Sigma}(\mathbf{k}, i\mathbf{k}_n)]^{-1}, \quad (5)$$

where $\hat{h}(\mathbf{k})$ represents the free part Hamiltonian including SOC [see Eq. (1)]. The self-energy is obtained by taking the derivative of Φ with respect to \hat{G} , i.e., plucking one line of Fig. 1 (c) to (f),

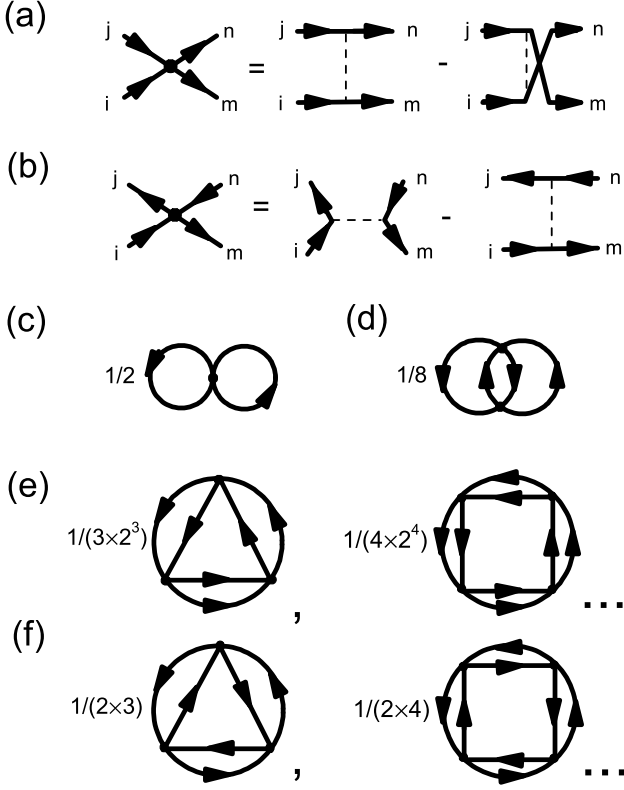


FIG. 1. (a) and (b) are bare Hugenholtz vertices for the PP and PH channels. (c) and (d) represent the HF term and the second order term. (e) and (f) are RPA forms of the closed linked Φ diagrams for the PP and PH channels. The numbers in front of diagrams (c)-(f) are the symmetry factors. Note that there are no anomalous Green's function lines because we only consider the normal state properties here.

$$\begin{aligned} \Sigma_{ij}(k) = & \frac{T}{N} \sum_{q;mn} \{ \Gamma_{ij,mn}^h G_{mn}(k-k') e^{i(k_l - k'_l)0^+} \\ & + 0.5 [\hat{\Gamma}^h \hat{\chi}^{h0}(q) \hat{\Gamma}^h]_{im,jn} G_{mn}(k-q) \\ & - [\hat{\Gamma}^p (\hat{\chi}^p(q) - \hat{\chi}^{p0}(q)) \hat{\Gamma}^p]_{in,jm} G_{mn}(q-k) \\ & + [\hat{\Gamma}^h (\hat{\chi}^h(q) - \hat{\chi}^{h0}(q)) \hat{\Gamma}^h]_{im,jn} G_{mn}(k-q) \}, \end{aligned} \quad (6)$$

where the abbreviation $k \equiv [\mathbf{k}, ik_l]$ ($q \equiv [\mathbf{q}, iq_l]$) is used with the fermion (boson) Matsubara frequency $k_l = (2l+1)\pi T$ ($q_l = 2l\pi T$). The first and second terms in Eq. (6) represent the HF and second order contributions, and the third and forth terms represent the RPA-bubbles of the PP and PH channels. The susceptibilities for these two channels are given by the $(2m)^2 \times (2m)^2$ matrices,

$$\begin{aligned} \hat{\chi}^p(q) &= \hat{\chi}^{p0}(q) [\hat{1} + \hat{\Gamma}^p \hat{\chi}^{p0}(q)]^{-1}, \\ \hat{\chi}^h(q) &= \hat{\chi}^{h0}(q) [\hat{1} + \hat{\Gamma}^h \hat{\chi}^{h0}(q)]^{-1}, \end{aligned} \quad (7)$$

in which the Linhard functions are defined respectively

by,

$$\begin{aligned} \chi_{ij,mn}^{p0}(q) &= \frac{T}{2N} \sum_k G_{im}(q-k) G_{jn}(k), \\ \chi_{ij,mn}^{h0}(q) &= -\frac{T}{N} \sum_k G_{im}(k+q) G_{nj}(k). \end{aligned} \quad (8)$$

Equations (5) to (8) form a closed set and thus could be solved self-consistently.

The irreducible vertex of the Bethe-Salpeter (BS) equation for the PH channel is the differentiation of self-energy (or the second derivative of Φ) with respect to \hat{G} . Apparently there are two kinds of contributions: (a) the diagrams in which the plucked two lines belong to the same bubble and only single RPA-form fluctuation is included. (b) Aslamazov-Larkin (AL) diagrams in which the plucked two lines belong to different bubbles and more than one RPA-form fluctuations are taken into account. Here we omit the AL diagrams for the following reasons^{17,18,28}: First, the AL contributions are demonstrated to be small (no more than 15% for the zero-momentum static susceptibility, for example). Second, the AL contributions will aggravate the agreement between the FLEX results and the benchmark QMC simulations. Third, the AL diagrams are necessary if we require keeping the conservation law rigorously, which is believed to be essential in some transport studies²⁹. Since here we investigate the equilibrium properties of electrons in the normal state, the AL diagrams can be safely removed. Therefore we obtain the PH channel's irreducible vertex

$$\begin{aligned} I_{ij,mn}^h(k, k'; Q) &= \Gamma_{ij,mn}^h - [\hat{\Gamma}^h \hat{\chi}^h(k-k') \hat{\Gamma}^h]_{im,jn} \\ &+ [\hat{\Gamma}^p \hat{\chi}^p(k+k'+Q) \hat{\Gamma}^p]_{in,jm}, \end{aligned} \quad (9)$$

where momenta k, k' are for the fermions and Q is for the collective bosonic mode. The corresponding BS equation reads

$$\begin{aligned} \sum_{k';\alpha\beta} I_{ij,\alpha\beta}^h(k, k'; Q) G_{\alpha m}(k'+Q) G_{n\beta}(k') \psi_{mn}^h(k'; Q) \\ = \lambda_Q^h \psi_{ij}^h(k; Q), \end{aligned} \quad (10)$$

where λ_Q^h and $\psi^h(k; Q)$ represent the eigenvalue and eigenfunction. Particularly, if λ_Q^h approaches to 1 at zero frequency, the system undergoes a spontaneously symmetry breaking at momentum Q in the PH channel.

The irreducible vertex for PP channel is the second derivative of Φ with respect to anomalous Green's functions \hat{F} and \hat{F}^\dagger ³⁰, here $F_{ij} = \langle T_\tau c_i c_j \rangle$ and $F_{ij}^\dagger = \langle T_\tau c_i^\dagger c_j^\dagger \rangle$. Although there is no anomalous Green's function lines in the original Φ diagrams (see Fig. 1), we can construct such diagrams by replacing two \hat{G} with \hat{F} and \hat{F}^\dagger but keeping two arrows pointing in and other two arrows pointing out at each dot. Here we omit the AL diagrams

again and obtain the PP channel's irreducible vertex

$$I_{ij,mn}^p(k, k'; Q) = \frac{1}{2} \Gamma_{ij,mn}^p - [\hat{\Gamma}^h \hat{\chi}^h(k - k') \hat{\Gamma}^h]_{im,nj}, \quad (11)$$

and the corresponding BS equation

$$\begin{aligned} - \sum_{k'; \alpha\beta} I_{ij, \alpha\beta}^p(k, k'; Q) G_{\alpha m}(k' + Q) G_{\beta n}(-k') \psi_{mn}^p(k'; Q) \\ = \lambda_Q^p \psi_{ij}^p(k; Q). \end{aligned} \quad (12)$$

Unlike the PH channel, the largest eigenvalue λ_Q^p always associates with $Q = [0, 0]$, indicating the formation of Cooper pairs with opposite momenta. Eqs. (11) and (12) can be used to investigate the most favorable superconducting pairing gap which corresponds to $\hat{\psi}^p(k; Q)$ with the largest value of λ_Q^p .

We have completed the introduction of the formal FLEX formulations, in practical application some reasonable approximations are widely used to simplify the computations. First, when the on-site interactions are all repulsive, the contributions of the PP RPA-bubbles in Fig. 1 (e) are relatively small and therefore could be safely left out^{17-19,31}. Second, it is more convenient to choose other numerical criterions, instead of Eq. (10), to evaluate the PH channel's instability. For example, one can choose the Stoner-like criterion $\det[\hat{1} + \hat{\Gamma}^h \hat{\chi}^{h0}(Q, 0)] < 0.002^{19}$, or if the biggest element of $\chi_{ij}^h(Q, 0)$ is 50 times larger than $\chi_{ij}^{h0}(Q, 0)^{23}$, as we employ in this paper.

To apply the above FLEX method to our study, the Hugenholtz vertices in Eq. (4) are fabricated by the on-site interactions (U, U, J, J') , and the results presented in this paper are given by the parameters $(U, U, J, J') = (5, 3.5, 0.75, 0.75)$, no qualitative different results are obtained when we change the values of U and J . The numerical calculations are performed on 64×64 \mathbf{k} meshes with 1024 (for $T = 0.04$), 2048 (for $T = 0.02, 0.015$) and 4096 (for $T = 0.01$) Matsubara frequencies. Particularly, we utilize the technique developed by Deisz *et al.*³² to efficiently include the contribution of high Matsubara frequencies. The analytical continuation of Green's functions to the real frequency is carried out by Padé approximation³³. The convergent solutions of the FLEX equations are obtained if the relative error of each matrix element of $\hat{\Sigma}$ is smaller than 10^{-6} .

III. RESULTS AND DISCUSSION

A. Collective excitations

Let us first define corresponding susceptibilities for various collective excitations relevant to the following discussions. The static transverse spin (TS) and longitudinal

spin (LS) susceptibilities are given by

$$\begin{aligned} \chi^{\text{TS}}(Q) &= \sum_{mn} \sum_{\alpha\beta\mu\nu} \sigma_{\alpha\beta}^x \sigma_{\mu\nu}^x \chi_{m\beta m\alpha, n\mu n\nu}^h(Q, 0), \\ \chi^{\text{LS}}(Q) &= \sum_{mn} \sum_{\alpha\beta\mu\nu} \sigma_{\alpha\beta}^z \sigma_{\mu\nu}^z \chi_{m\beta m\alpha, n\mu n\nu}^h(Q, 0), \end{aligned} \quad (13)$$

where the spin and orbital degrees of freedom have been expressed by $(\alpha, \beta, \mu, \nu)$ and (m, n) , respectively. The charge fluctuation is too small compared to other fluctuations and thus is not discussed here. Because of the introduction of SOC, the contribution of orbital fluctuations is no longer neglectable, so we define the static transverse orbital (TO) and longitudinal orbital (LO) susceptibilities

$$\begin{aligned} \chi^{\text{TO}}(Q) &= \sum_{\alpha\beta} \sum_{ijmn} L_{ij}^x L_{mn}^x \chi_{j\alpha i\alpha, m\beta n\beta}^h(Q, 0), \\ \chi^{\text{LO}}(Q) &= \sum_{\alpha\beta} \sum_{ijmn} L_{ij}^z L_{mn}^z \chi_{j\alpha i\alpha, m\beta n\beta}^h(Q, 0). \end{aligned} \quad (14)$$

As discussed in the introduction, it has been suggested that the low-energy physics in Sr_2IrO_4 may be described as an effective one-band model with the isospin $J_{\text{eff}} = 1/2^{11,12}$. To check its possible application here, we define the isospin susceptibility. The creation operators for the isospin-up and isospin-down states with momentum \mathbf{k} are given by $a_{\mathbf{k}, \uparrow}^\dagger = (d_{\mathbf{k}, 1, \downarrow}^\dagger + id_{\mathbf{k}, 2, \downarrow}^\dagger + d_{\mathbf{k}, 3, \uparrow}^\dagger)/\sqrt{3}$ and $a_{\mathbf{k}, \downarrow}^\dagger = (d_{\mathbf{k}, 1, \uparrow}^\dagger - id_{\mathbf{k}, 2, \uparrow}^\dagger - d_{\mathbf{k}, 3, \downarrow}^\dagger)/\sqrt{3}$, where indexes 1, 2, 3 denote yz , zx , and xy orbitals. Therefore, the isospin operator can be constructed: $S_q^\alpha = \sum_{\mathbf{k}} (a_{\mathbf{k}+\mathbf{q}, \uparrow}^\dagger, a_{\mathbf{k}+\mathbf{q}, \downarrow}^\dagger) \boldsymbol{\sigma}^\alpha (a_{\mathbf{k}, \uparrow}, a_{\mathbf{k}, \downarrow})^T$. Then, the static transverse isospin (TI) and longitudinal isospin (LI) susceptibilities are given by,

$$\begin{aligned} \chi^{\text{TI}}(Q) &= \frac{T}{N} \int_0^{\frac{1}{T}} \langle T_\tau S^x(\mathbf{q}, \tau) S^x(-\mathbf{q}, 0) \rangle d\tau, \\ \chi^{\text{LI}}(Q) &= \frac{T}{N} \int_0^{\frac{1}{T}} \langle T_\tau S^z(\mathbf{q}, \tau) S^z(-\mathbf{q}, 0) \rangle d\tau. \end{aligned} \quad (15)$$

The static TS, LS, TO and LO susceptibilities for 3% electron-doping at $T = 0.01$ are shown in Fig. 2 (a)-(d). As expected, the strong peaks exist around $(\pm\pi, \pm\pi)$, which are reminiscences of the AFM order in the parent compound. In particular, the intensities of orbital susceptibilities are all stronger than those of spin susceptibilities, and the TO fluctuation overwhelms the LO fluctuation. These features are consistent with the experimental results in the single-crystal neutron diffraction⁴ and nonresonant magnetic X-ray diffraction³⁴.

Fig. 2 (e) and (f) show the TI and LI susceptibilities for the same 3% electron doping at $T = 0.01$. The peaks also reside at the same momenta as in the spin and orbital fluctuations. Quite strikingly, the intensity of the TI susceptibility is almost one order of magnitude larger than that of all other fluctuations. To show in more detail the

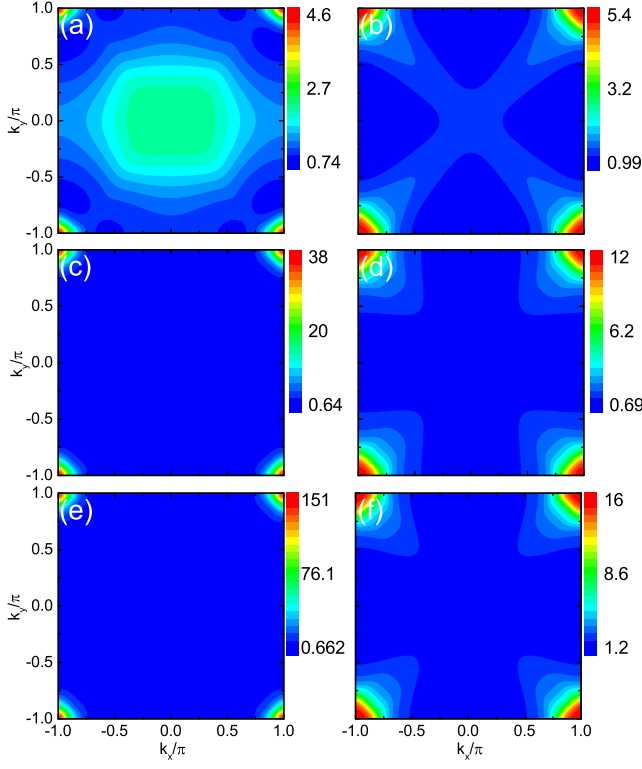


FIG. 2. (Color online) Susceptibility for various collective excitations at 3% electron-doping and $T = 0.01$. (a), (b), (c) and (d) show static TS, LS, TO and LO susceptibilities, respectively. (e) and (f) show static TI and LI susceptibilities (see text). The TS fluctuation in (a) no longer exhibits the C_4 symmetry with the introduction of SOC.

effects of the isospin fluctuations, in Fig. 3 (a) we compare the maximum magnitude of $\chi^\alpha(\mathbf{q})$ at $T = 0.02$, from 40% hole-doping to 30% electron-doping, with α denoting TI, LI, TO, LO, TS and LS channels. The AFM order is determined by the numerical criterion in the PH channel, as introduced in Sec. II B. As shown, the TI susceptibility tends to diverge as the system approaches the AFM state, from both the electron-doped side and the hole-doped side. These results suggest that the AFM order in the undoped and slightly doped system is mainly caused by the TI fluctuation. Consequently, it shows that the effective one-band model with the isospin $J_{\text{eff}} = 1/2$ ^{11,12} can describe the magnetic properties reasonably in the undoped and slightly doped Sr_2IrO_4 . Another feature drawn from Fig. 3 (a) is that the AFM is more robust against the hole-doping in comparison to the electron-doping, which may be useful for the related experimental investigations.

When the system is doped away from the AFM region, Fig. 3 (a) shows that the TI fluctuation decreases rapidly with doping. However, it still has larger magnitude than all others in the region of 30% hole-doping to 50% electron-doping (the results for $> 30\%$ electron-doping are not shown here), though their differences are decreased with dopings. In this region, the momentum \mathbf{q}

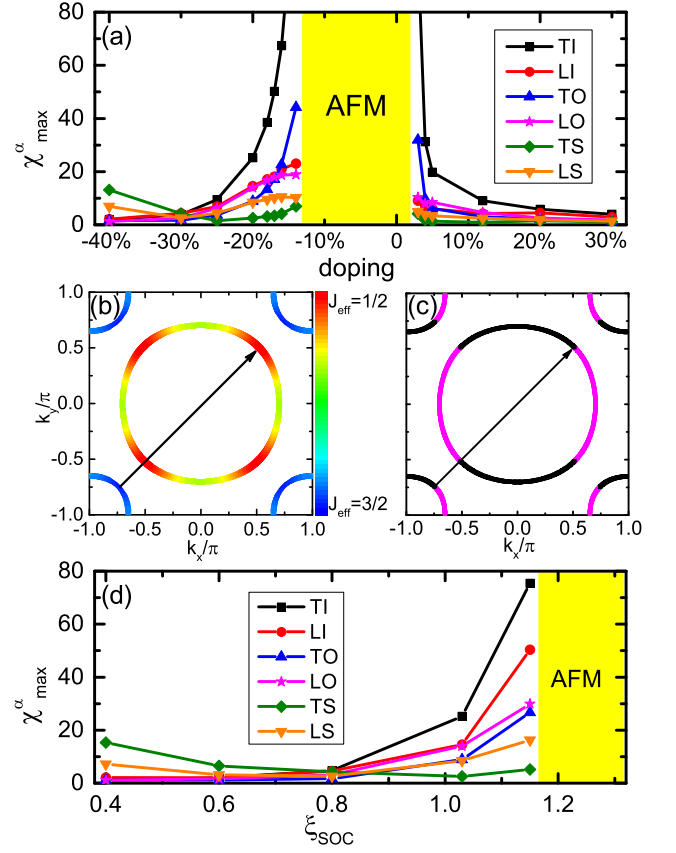


FIG. 3. (Color online) (a) The largest value of various susceptibilities $\chi^\alpha(\mathbf{q})$ as a function of electron doping (positive) and hole doping (negative) at $T = 0.02$, with $\alpha = \text{TI, LI, TO, LO, TS or LS}$. (b) Fermi surfaces for 40% hole doping with the different colors representing the weights of the $J_{\text{eff}} = 1/2$ doublet and $J_{\text{eff}} = 3/2$ quartet. (c) The same as (b), but with the colors indicating the majority orbital character (magenta: d_{xz} , black: d_{yz}). (d) The largest value of $\chi^\alpha(\mathbf{q})$ as a function of the SOC magnitude ξ_{SOC} at $T = 0.02$ for 20% hole doping. The lines with an arrow in (b) and (c) indicate the nesting vector.

is at or near the (π, π) point. When doping the system further with holes ($> 30\%$), the spin fluctuation becomes dominant so that the effective one-band picture is broken down. These results can be understood from the weights of the $J_{\text{eff}} = 1/2$ doublet and $J_{\text{eff}} = 3/2$ quartet along the Fermi surface, as shown in Fig. 3 (b). One can see that the closed electron pocket centered around the $\Gamma = (0, 0)$ point is composed mainly of the $J_{\text{eff}} = 1/2$ doublet, while the hole pocket around (π, π) mainly of the $J_{\text{eff}} = 3/2$ quartet. For 40% hole-doping, the hole Fermi pocket becomes large and introduces a Fermi surface nesting between the hole and electron pockets, as shown in Fig. 3 (b). Thus, the inter-pocket particle-hole scattering between the $J_{\text{eff}} = 1/2$ dominant band and $J_{\text{eff}} = 3/2$ dominant band takes action and overwhelms the intra-pocket scattering in the $J_{\text{eff}} = 1/2$ dominant band, which makes the isospin fluctuation no longer the

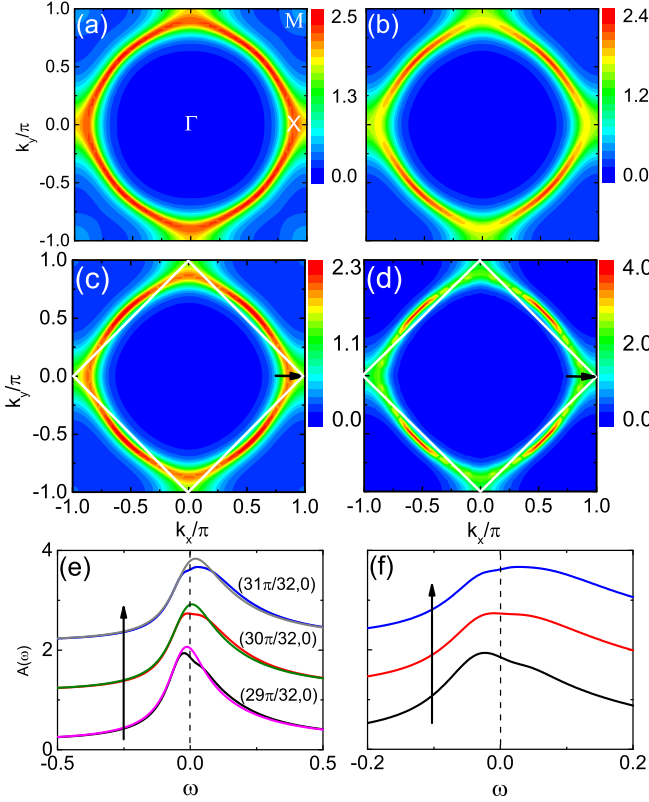


FIG. 4. (Color online) Spectral functions $A(\mathbf{k}, 0)$ for 10% electron-doping (a) and 5% electron-doping (b) at $T = 0.015$. Spectral functions $A(\mathbf{k}, 0)$ at $T = 0.02$ (c) and $T = 0.01$ (d) for 3% electron-doping. The pink (black), green (red), gray (blue) lines in (e) are ω dependence of the spectral functions for $T = 0.02$ ($T = 0.01$), at three momenta indicated by the arrow in (c) and (d). An enlarged version for $T = 0.01$ is shown in (f). The white lines in (c) and (d) denote the boundary of the magnetic Brillouin zone.

leading collective excitation. On the other hand, from the distribution of orbital characters shown in Fig. 3 (c), we can find that the main inter-pocket scattering occurs in the same orbital, which makes the orbital fluctuations also suppressed. Therefore, the spin fluctuation is the dominant collective excitation for the heavily hole-doped system. However, the Fermi level moves away from the $J_{\text{eff}} = 3/2$ dominant band with the electron doping, consequently it is only the $J_{\text{eff}} = 1/2$ dominant band that crosses the Fermi level. Therefore, the one-band picture is always robust against the electron doping. Furthermore, we have also examined the range of validity of the effective one-band picture with respect to the strength of SOC. As shown in Fig. 3 (d), the TI susceptibility prevails all others for 20% hole-doping if $\xi_{\text{SOC}} > 0.8$, indicating that this picture survives in an extended range.

B. Weak pseudogap behavior and Fermi arcs

The pseudogap behavior can be detected from the single particle spectral function which is defined as $A(\mathbf{k}, \omega) = -\sum_n \text{Im} G_{nn}(\mathbf{k}, \omega)/\pi$, where n denotes both spin and orbital indices. In Fig. 4 (a) and (b), we show the contour plot of the zero-energy spectrum at $T = 0.015$ for 10% and 5% electron-doping, respectively. Since the system has been away from the AFM order at these dopings [see Fig. 3 (a)], an intact Fermi surface is expected in the conventional normal state. Indeed, for 10% electron-doping, a closed diamond-shaped Fermi surface is observed, as shown in Fig. 4 (a). However, an obvious reduction in the spectral intensity occurs around $(0, \pi)$ and its symmetric points for 5% electron-doping. This reduction is strongly temperature-dependent, because it appears only below a certain temperature, as shown in Fig. 4 (c) and (d) at 3% electron-doping for $T = 0.02$ and $T = 0.01$, respectively. Owing to the suppression of the spectra near $(0, \pm\pi)$ and $(\pm\pi, 0)$, the Fermi surface around these momenta is destructed and the four residual separated segments form the so-called Fermi arcs [see Fig. 4 (b) and (d)]. These results are consistent with the recent ARPES experiment⁸. In order to look in more detail the suppression of the spectra, we show the energy distribution curves (EDC) of the spectral functions for 3% electron-doping at three momentum points near $(\pi, 0)$ in Fig. 4 (e). One can see that the suppression occurs basically around the Fermi energy when the temperature is decreased from $T = 0.02$ to $T = 0.01$. Moreover, different from a well defined quasiparticle peak at $T = 0.02$, the spectral functions at $T = 0.01$ for $\mathbf{q} = (30\pi/32, 0)$ and $(31\pi/32, 0)$ show a weak dip around the Fermi energy, as shown in Fig. 4 (f). It suggests that a weak pseudogap does exist around $(\pi, 0)$ and its symmetric momenta for slightly electron-doping.

Since there is no long-range order in this doping range, the pseudogap is most likely to result from the scattering of quasiparticles by the collective excitations. In this framework, the quasiparticles around $(\pi, 0)$ and $(0, \pi)$ are strongly coupled by the collective excitations with the transferred momentum (π, π) in the scattering process. In accord with this analysis, the results presented in Fig. 2 demonstrate that all collective excitations, including the spin, orbital and isospin fluctuations, exhibit the characteristic momentum (π, π) . In particular, the transverse isospin (TI) fluctuation overwhelms the spin and orbital fluctuations. We have also carried out a careful examination, and find that all the important elements of $\hat{\chi}^h(\mathbf{q}, 0)$ are included in the TI fluctuation. Especially, for $\mathbf{q} = (\pi, \pi)$ the elements included in the TI susceptibility are calculated to amount to 91.3% weight of the total PH susceptibilities for 3% electron-doping at $T = 0.01$. Therefore, it suggests that the scatterings of quasiparticles by the (π, π) TI fluctuation lead to a weak pseudogap partially opened around $(0, \pm\pi)$ and $(\pm\pi, 0)$.

We have also investigated the possible pseudogap be-

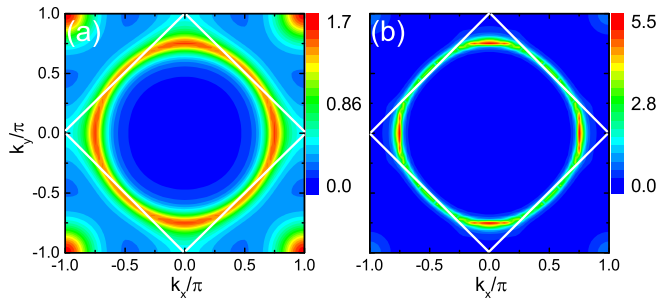


FIG. 5. (Color online) (a) and (b) are spectral functions $A(\mathbf{k}, 0)$ at $T = 0.04$ and $T = 0.01$ for 17% hole-doping. The white lines denote the boundary of the magnetic Brillouin zone.

havior and Fermi arcs in the lightly hole-doped region. The typical results of the spectral function $A(\mathbf{k}, 0)$ for 17% hole-doping are shown in Fig. 5. At $T = 0.04$, there is a nearly circular Fermi surface around the Γ point. By decreasing the temperature to $T = 0.01$, the spectral weights are suppressed on some Fermi momenta and consequently it leads to the formation of the Fermi arcs. However, the suppressions now appear around $(\pi/2, \pi/2)$, which is contrary to the case of the electron-doping shown in Fig. 4 (b) and (d). This suppression also results from the (π, π) TI fluctuation. In this case, the Fermi surface shrinks in comparison with that of electron-doping, so that the “hot spots” (the crossing points of the Fermi surface with the boundary of the AFM Brillouin zone) at which the quasiparticles are strongly scattered move from the $(\pm\pi, 0)$ and $(0, \pm\pi)$ points to the

$(\pm\pi/2, \pm\pi/2)$ points (see Fig. 4 and Fig. 5).

IV. SUMMARY

In summary, we have extended the FLEX approach by Hugenholtz diagrams to include the case where $SU(2)$ symmetry is broken. Using this approach, we investigate various collective fluctuations and the spectral function of quasiparticles. It is found that the isospin fluctuations derived from the $J_{\text{eff}} = 1/2$ spin-orbit Mott insulator dominate over the spin, orbital and charge fluctuations in the extended doping region, suggesting the validity of the isospin $J_{\text{eff}} = 1/2$ picture in an extended doping regime. Also the isospin fluctuation leads to the emergence of the pseudogap and Fermi arcs in the slightly doped system, which is consistent with the ARPES experiments for slightly doped Sr_2IrO_4 ^{8,10}.

ACKNOWLEDGMENTS

We would like to acknowledge Q. H. Wang and H. Y. Zhang for discussions on the generalized FLEX method, H. Yao and J. Kang for their useful discussions. This work was supported by the National Natural Science Foundation of China (11190023, 11204125 and 11404163), the Ministry of Science and Technology of China (973 Project Grants No.2011CB922101 and No. 2011CB605902).

¹ For a review see W. Witczak-Krempa, G. Chen, Y. B. Kim, and L. Balents, *Annu. Rev. Condens. Matter Phys.* **5**, 57 (2014).

² D. Pesin and L. Balents, *Nature Phys.* **6**, 376 (2010); Y. Machida, S. Nakatsuji, S. Onoda, T. Tayama, and T. Sakakibara, *Nature (London)* **463**, 210 (2010); X. Wan, A. M. Turner, A. Vishwanath, and S. Y. Savrasov, *Phys. Rev. B* **83**, 205101 (2011); X. Liu, T. Berlijn, W.-G. Yin, W. Ku, A. Tsvelik, Y.-J. Kim, H. Gretarsson, Y. Singh, P. Gegenwart, and J. P. Hill, *Phys. Rev. B* **83**, 220403 (2011); F. Ye, S. Chi, H. Cao, B. C. Chakoumakos, J. A. Fernandez-Baca, R. Custelcean, T. F. Qi, O. B. Korneta, and G. Cao, *Phys. Rev. B* **85**, 180403(R) (2012); Y. Singh, S. Manni, J. Reuther, T. Berlijn, R. Thomale, W. Ku, S. Trebst, and P. Gegenwart, *Phys. Rev. Lett.* **108**, 127203 (2012); Z. Alpichshev, F. Mahmood, G. Cao, and N. Gedik, *Phys. Rev. Lett.* **114**, 017203 (2015).

³ M. K. Crawford, M. A. Subramanian, R. L. Harlow, J. A. Fernandez-Baca, Z. R. Wang, and D. C. Johnston, *Phys. Rev. B* **49**, 9198 (1994); F. Ye, S. Chi, B. C. Chakoumakos, J. A. Fernandez-Baca, T. Qi, and G. Cao, *Phys. Rev. B* **87**, 140406(R) (2013).

⁴ Q. Huang, J. L. Soubeyroux, O. Chmaissem, I. Natali Sora, A. Santoro, R. J. Cava, J. J. Krajewski, and W. F. Peck,

Jr., *J. Solid State Chem.* **112**, 355 (1994); G. Cao, J. Bolivar, S. McCall, J. E. Crow, and R. P. Guertin, *Phys. Rev. B* **57**, R11039(R) (1998).

⁵ J. Kim, D. Casa, M. H. Upton, T. Gog, Y. J. Kim, J. F. Mitchell, M. van Veenendaal, M. Daghofer, J. van den Brink, G. Khaliullin, and B. J. Kim, *Phys. Rev. Lett.* **108**, 177003 (2012); S. Bahr, A. Alfonsov, G. Jackeli, G. Khaliullin, A. Matsumoto, T. Takayama, H. Takagi, B. Büchner, and V. Kataev, *Phys. Rev. B* **89**, 180401 (2014).

⁶ Y. Liu et al., e-print arXiv:1501.04687v1.

⁷ F. Wang and T. Senthil, *Phys. Rev. Lett.* **106**, 136402 (2011); H. Watanabe, T. Shirakawa, and S. Yunoki, *Phys. Rev. Lett.* **110**, 027002 (2013); Y. Yang, W.-S. Wang, J.-G. Liu, H. Chen, J.-H. Dai, and Q.-H. Wang, *Phys. Rev. B* **89**, 094518 (2014); Z. Y. Meng, Y. B. Kim, and H.-Y. Kee, *Phys. Rev. Lett.* **113**, 177003 (2014).

⁸ Y. K. Kim, O. Krupin, J. D. Denlinger, A. Bostwick, E. Rotenberg, Q. Zhao, J. F. Mitchell, J. W. Allen, and B. J. Kim, *Science* **345**, 187 (2014).

⁹ D. S. Marshall, D. S. Dessau, A. G. Loeser, C.-H. Park, A. Y. Matsuura, J. N. Eckstein, I. Bozovic, P. Fournier, A. Kapitulnik, W. E. Spicer, and Z.-X. Shen, *Phys. Rev. Lett.* **76**, 4841 (1996); A. G. Loeser, Z.-X. Shen, D. S. Dessau, D. S. Marshall, C. H. Park, P. Fournier, and A. Kapitul-

- nik, *Science* **273**, 325 (1996); H. Ding, T. Yokoya, J. C. Campuzano, T. Takahashi, M. Randeria, M. R. Norman, T. Mochiku, K. Kadowaki, and J. Giapintzakis, *Nature (London)* **382**, 51 (1996).
- ¹⁰ Y. Cao, Q. Wang, J. A. Waugh, T. J. Reber, H. Li, X. Zhou, S. Parham, N. C. Plumb, E. Rotenberg, A. Bostwick, J. D. Denlinger, T. Qi, M. A. Hermele, G. Cao, and D. S. Dessau, arXiv: 1406.4978 (2014).
 - ¹¹ B. J. Kim, H. Jin, S. J. Moon, J.-Y. Kim, B.-G. Park, C. S. Leem, J. Yu, T.W. Noh, C. Kim, S.-J. Oh, J.-H. Park, V. Durairaj, G. Cao, and E. Rotenberg, *Phys. Rev. Lett.* **101**, 076402 (2008).
 - ¹² B. J. Kim, H. Ohsumi, T. Komesu, S. Sakai, T. Morita, H. Takagi and T. Arima, *Science* **323**, 1329 (2009).
 - ¹³ D. Hsieh, F. Mahmood, D. H. Torchinsky, G. Cao, and N. Gedik, *Phys. Rev. B* **86**, 035128 (2012).
 - ¹⁴ R. Arita, J. Kunes, A. V. Kozhevnikov, A. G. Eguiluz, and M. Imada, *Phys. Rev. Lett.* **108**, 086403 (2012).
 - ¹⁵ X. Liu, V. M. Katukuri, L. Hozoi, W.-G. Yin, M. P. M. Dean, M. H. Upton, J. Kim, D. Casa, A. Said, T. Gog, T. F. Qi, G. Cao, A. M. Tsvelik, J. van den Brink, and J. P. Hill, *Phys. Rev. Lett.* **109**, 157401 (2012).
 - ¹⁶ Q. Li, G. Cao, S. Okamoto, J. Yi, W. Lin, B. C. Sales, J. Yan, R. Arita, J. Kunes, A. V. Kozhevnikov, A. G. Eguiluz, M. Imada, Z. Gai, M. Pan, and D. G. Mandrus, *Sci. Rep.* **3**, 3073 (2013).
 - ¹⁷ N. E. Bickers, D. J. Scalapino, and S. R. White, *Phys. Rev. Lett.* **62**, 961(1989); N. E. Bickers and D. J. Scalapino, *Ann. Phys. (N.Y.)* **193**, 206 (1989).
 - ¹⁸ N. E. Bickers and S. R. White, *Phys. Rev. B* **43**, 8044 (1991).
 - ¹⁹ T. Takimoto, T. Hotta, and K. Ueda, *Phys. Rev. B* **69**, 104504 (2004).
 - ²⁰ T. Dahm, L. Tewordt, and S. Wernbter, *Phys. Rev. B* **49**, 748 (1994); M. Langer, J. Schmalian, S. Grabowski, and K. H. Bennemann, *Phys. Rev. Lett.* **75**, 4508 (1995); A. I. Liechtenstein, O. Gunnarsson, O. K. Andersen, and R. M. Martin, *Phys. Rev. B* **54**, 12505 (1996); J. J. Deisz, D. W. Hess, and J. W. Serene, *Phys. Rev. Lett.* **76**, 1312 (1996); J. R. Engelbrecht, A. Nazarenko, M. Randeria, and E. Dagotto, *Phys. Rev. B* **57**, 13406 (1998); X.-Z. Yan and C. S. Ting, *Phys. Rev. Lett.* **97**, 067001 (2006).
 - ²¹ Z. J. Yao, J. X. Li, and Z. D. Wang, *New J. Phys.* **11**, 025009 (2009); S. L. Yu, J. Kang, and J. X. Li, *Phys. Rev. B* **79**, 064517 (2009); H. Ikeda, R. Arita, and J. Kuneš, *Phys. Rev. B* **82**, 024508 (2010); S. Onari and H. Kontani, *Phys. Rev. B* **85**, 134507 (2012).
 - ²² J. J. Deisz, D. W. Hess, and J. W. Serene, *Phys. Rev. B* **66**, 014539 (2002); M. Mochizuki, Y. Yanase, and M. Ogata, *Phys. Rev. Lett.* **94**, 147005 (2005); Z. J. Yao, J. X. Li, and Z. D. Wang, *Phys. Rev. B* **76**, 212506. (2007); J. Kang, S. L. Yu, Z. J. Yao and J. X. Li, *J. Phys.: Condens. Matter* **23**, 175702 (2011); B. Horváth, B. Lazarovits and G. Zaránd, *Phys. Rev. B* **84**, 205117, (2011).
 - ²³ H. Wang, S. L. Yu and J. X. Li, *Phys. Lett. A* **378**, 3360 (2014).
 - ²⁴ H. Watanabe, T. Shirakawa, and S. Yunoki, *Phys. Rev. Lett.* **105**, 216410 (2010).
 - ²⁵ G. Baym and L. P. kadanoff, *Phys. Rev.* **124**, 287 (1961); G. Baym, *Phys. Rev.* **127**, 1391 (1962).
 - ²⁶ J. M. Luttinger and J. C. Ward, *Phys. Rev.* **118**, 1417 (1960).
 - ²⁷ J. W. Negele, and H. Orland, *Quantum Many-Particle Systems* (Addison-Wesley, Reading, MA, 1987), Section 2.3.
 - ²⁸ N. E. Bickers, *Self-Consistent Many-Body Theory for Condensed Matter Systems*, edited by D. Sénéchal et al., (Springer New York, 2004) chapter 6.
 - ²⁹ L. P. Kadanoff and G. Baym, *Quantum Statistical Mechanics* (Benjamin, Menlo Park, CA 1962), chapter 10.
 - ³⁰ L. Tewordt, *J. Low Temp. Phys.* **15**, 349 (1974).
 - ³¹ Indeed, we have checked that our calculations show no qualitative differences with or without PP RPA-bubbles.
 - ³² J. J. Deisz, D. W. Hess, and J. W. Serene, *Recent Progress in Many-Body Theories*, edited by E. Schachinger et al. (Plenum Press, New York, 1995), Vol. 4.
 - ³³ H. J. Vidberg and J. W. Serene, *J. Low Temp. Phys.* **29**, 179 (1977).
 - ³⁴ S. Fujiyama, H. Ohsumi, K. Ohashi, D. Hirai, B. J. Kim, T. Arima, M. Takata, and H. Takagi, *Phys. Rev. Lett.* **112**, 016405 (2014).